IEEE Access
Multidisciplinary | Rapid Review | Open Access Journal

Received November 10, 2019, accepted November 23, 2019, date of publication November 28, 2019,
date of current version December 16, 2019.

Digital Object Identifier 10.1109/ACCESS.2019.2956499

Electromagnetic Signature of a Quadcopter Drone and Its Relationship With Coupling Mechanisms

SANGIN KIM[1], (Student Member, IEEE), YEONG-HOON NOH[1], JINHYO LEE[1], JONGWON LEE[2], (Member, IEEE), JIN-SOO CHOI[2], AND JONG-GWAN YOOK[1], (Senior Member, IEEE)

[1]Department of Electrical and Electronic Engineering, Yonsei University, Seoul 03722, South Korea
[2]Agency for Defense Development, Daejeon 34186, South Korea

Corresponding author: Jong-Gwan Yook (jgyook@yonsei.ac.kr)

This work was supported by the Agency for Defense Development.

ABSTRACT This paper presents an investigation of the electromagnetic signature and the coupling mechanism of quadcopter drones with incident electromagnetic (EM) wave and radar cross section (RCS) analysis. Coupling analysis is performed based on the dominant coupling path: when an incident EM wave with a magnitude of 50 kV/m contacts a commercial quadcopter drone, its motor power wires are identified as the dominant coupling path. Higher coupling voltages are obtained for frequencies that have large impedance values at both ends of the load on the motor power wire. This induced voltage can affect the integrated circuit chip on a printed circuit board, as well as parallel plate resonances. Furthermore, the RCS of a quadcopter drone is measured in the frequency range of 0.5–3 GHz. The internal-component vulnerability characteristics of quadcopters can spike at specific frequencies with high RCS values and can be analyzed with or without motor power wires. We verified these hypotheses via 2D inverse synthetic aperture radar images, and we analyzed the results by comparing the empirical and full-wave simulation values.

INDEX TERMS Coupling analysis, input impedance, inverse synthetic aperture radar, parallel plate resonance, quadcopter drone, radar cross section, vulnerable path, wire coupling.

I. INTRODUCTION

The potential for high-power electromagnetic (HPEM) field attacks is ever increasing worldwide owing to easy access to high-power electrical sources. The potential damage to social infrastructure caused by HPEM attacks is significant [1]. Therefore, sensitive electronic devices and systems should be designed by using various shielding technologies with an aim to prevent possible damage from external electromagnetic (EM) waves [2]. The degree of influence of an EM wave varies based on the type of target electronic device. In general, most commercial devices such as computers and mobile devices utilize printed circuit boards (PCBs) containing various sensitive integrated circuits (ICs). For computers, conductive cases are used to enclose various electronic parts. Nevertheless, external EM waves can be designed to penetrate through apertures in these cases with transmission characteristics based on the characteristics of such apertures [3], [4]. Transmission characteristics are a function of various parameters such as the polarization, frequency, and incident direction of EM waves. A few studies have been conducted to estimate the threshold voltages that cause malfunctions in electronic devices. To prevent possible damage, various shielding methods against radiated emissions have been developed, including the use of a waveguide-below-cutoff array (WBCA), honeycomb structure, shielding window, or multilayered WBCA [5]–[10]. To suppress conducted emissions such as over-current, decoupling capacitors and diodes can be used during PCB fabrication [11]–[13].

Although there have been many extensive experimental studies on the susceptibility of electronic components and systems, few studies have focused on the coupling mechanisms from radiated emissions. Therefore, in this study, a commercial drone was selected as an example system to quantify coupling based on detailed three-dimensional (3D) full-wave EM modeling. Due to their composition of lightweight non-conductive materials, the radar cross sections (RCSs) of such drones are typically very small.

The associate editor coordinating the review of this manuscript and approving it for publication was Mohamed Kheir.

Many previous studies have focused on the detection of drones [14]–[17]. One such study developed a method for improving the quality of images based on the digital signal processing (DSP) of the extracted RCS of a drone, which was measured using an antenna operating at a specific center frequency, such as the X-band [18]. This type of technique relies on the measured RCS values of a drone. If the characteristics of a drone can be analyzed to determine frequencies that would result in high RCS values, it would be possible to obtain high-resolution data without relying on DSP.

In this study, a quadcopter drone composed of mechanical elements, blades, and motors for flight, and electronic elements on a flight-control PCB were thoroughly analyzed. Additionally, high-frequency circuit simulations were used to derive coupling waveforms based on various load conditions resulting from motor and PCB input characteristics. Furthermore, the vulnerability characteristics of the drone were analyzed to determine the frequencies with high RCS values based on its internal composition.

This article presents the results of our susceptibility analysis of a commercial quadcopter drone under the influence of external EM fields. Section II describes wire coupling mechanisms and the use of input impedances to derive port voltages. Section III presents an analysis of the PCB resonance phenomenon and the calculation of internal voltage waveforms. Section IV describes the RCS measurement data and the derived 2D inverse synthetic aperture radar (ISAR) images of the quadcopter used for the analysis of RCS vulnerability.

II. COUPLING PATH THROUGH A QUADCOPTER DRONE

When an external EM wave is incident onto a quadcopter drone, there exist various possible coupling paths depending on the component in the quadcopter. An EM field can be particularly effectively in coupling with the antenna, aperture, and wires, which can consequently affect various IC chips on the main PCB. In this section, vulnerable coupling paths are identified and the coupling strength is derived based on the type of incident EM wave.

A. WIRE COUPLING PATH

Fig. 1 presents the basic components of a commercial quadcopter drone. The main PCB, which is responsible for signal processing, control, and communication between the user and drone, is connected to four flight motors by wires. These motors receive operational commands and DC power from the main PCB located at the center of the quadcopter. Typically, two wires connect each of the four edges of the main PCB to the motors, as shown in Fig. 1.

When an EM wave is incident on the 2-wire, as shown in Fig. 2 (a), a portion of the energy is transferred into the wire based on various parameters. In this study, L and s are used to denote the length of and gap between the 2-wire, respectively, while R_S and R_L are used to denote the impedance on the left and right sides of the 2-wire, respectively. Incident E- and H-fields can be modeled as equivalent current and voltage

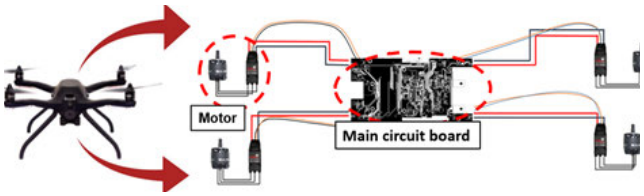

FIGURE 1. Main composition of a quadcopter drone.

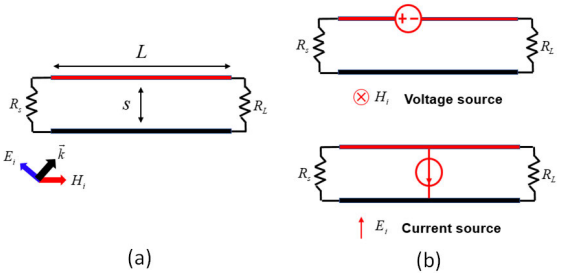

FIGURE 2. (a) Configuration of 2-wire coupling. (b) Voltage and current source according to an incident EM wave.

sources, respectively, as illustrated in Fig. 2 (b). In other words, an E-field is equivalent to a current source and has a maximized effect when a plane wave is incident perpendicularly to the 2-wire. An H-field is equivalent to a voltage source and has a maximized effect when a wave is incident parallelly to the 2-wire. The characteristics of coupling sources are determined by the magnitude and incident angle of an EM wave, as well as the physical dimensions and electrical properties of the 2-wire in case of electrically short lines. Equations (1) and (2) define the induced coupling voltages at the load end of the 2-wire [19].

$$\begin{aligned} V_S &= j\omega sL\frac{R_S}{R_S+R_L}\left(\mu_0 H^i - R_L c E^i\right) \\ &= j\omega sLE^i\frac{R_S}{R_S+R_L}\left(\frac{1}{c_0} - R_L c\right), \end{aligned} \tag{1}$$

$$\begin{aligned} V_L &= j\omega sL\frac{R_L}{R_S+R_L}\left(-\mu_0 H^i - R_S c E^i\right) \\ &= j\omega sLE^i\frac{R_L}{R_S+R_L}\left(-\frac{1}{c_0} - R_S c\right), \end{aligned} \tag{2}$$

$$c = \pi\epsilon ln\left(\frac{r_w}{s}\right), \tag{3}$$

where ω is the angular frequency, μ_0 is the permeability, c_0 is the velocity of light, E^i is the magnitude of the electric field, H^i is the magnitude of the magnetic field, and r_w is the diameter of wire. Because the terminal voltages can be calculated for electrically short lines, the per-unit-length elements and sources are multiplied by the total line length L. Clearly, coupling voltage amplitude is proportional to the magnitude and frequency of the incident wave. Additionally, the coupling amounts are functions of the 2-wire parameters. When the gap between the 2-wire s, length of the 2-wire L, and dielectric constant of the surrounding medium ϵ increase, the coupling amount increases proportionally [20]. Notably,

as R_S and R_L increase, the voltage due to the coupled current also increases over a large impedance. This occurs because the 2-wire system behaves as an antenna when the load impedance increases at both ends of the wire. The impedance values of the load can vary depending on the frequency of an incident wave. In the case of a quadcopter drone, because the physical parameters of the 2-wire (i.e., s and L) are fixed, the electrical parameters R_S and R_L, as well as the frequency of the incident wave, affect the induced voltage as shown in Equations (1) and (2). Field-to-circuit coupling is also possible in the transmission lines of the main PCB [21]. However, the physical dimensions s and L of the lines in the PCB are much smaller than those of the motor power wires. Therefore, 2-wire coupling through the motor power wires is much more relevant and must be carefully analyzed.

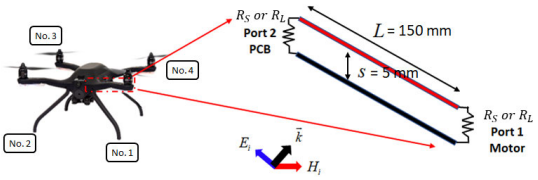

FIGURE 3. 2-wire coupling configuration in a quadcopter drone.

B. CHARACTERISTIC FREQUENCIES FOR WIRE COUPLING

A quadcopter drone contains four motors that are connected to the power and ground planes of the main PCB at each of the four edges via 2-wire lines. Therefore, the load and source impedances (R_S and R_L, respectively) of the 2-wire act as the input impedances for the PCB and motor sides, respectively, as illustrated in Fig. 3. Based on these impedance values, the coupling amounts at R_S and R_L can be calculated accurately [22]. Although the quadcopter model considered in this study (Blueye-1K model that contains acrylonitrile butadiene styrene (ABS) by HUINS) has very specific characteristics, the proposed methodology is valid for similar drones. Fig. 4 presents the measurement setup for measuring the input impedances of both the PCB and motor. Because the target system is a quadcopter drone, the input impedance of the PCB was measured at four different locations, as indicated in Fig. 4 (a). To measure the input impedance, each motor power wire to the main PCB was disconnected and an SMA connector was mounted on the PCB edge while the remaining motor power wires were connected. Subsequently, the input impedance was measured using a vector network analyzer (VNA) for the range of 0.3–3 GHz. The line type results, as shown in Fig. 5, present the measured input impedances observed at four locations on the PCB. The input impedances spike at specific frequencies, which are approximately 0.85 GHz and 2.7 GHz. The port impedances at all the wire locations exhibit similar frequency behavior, even though the PCB is not perfectly symmetric. It is possible that at these frequencies, the PCB can radiate a significant amount of signal or noise. Alternatively, the PCB could be particularly susceptible to external signals at these frequencies [23].

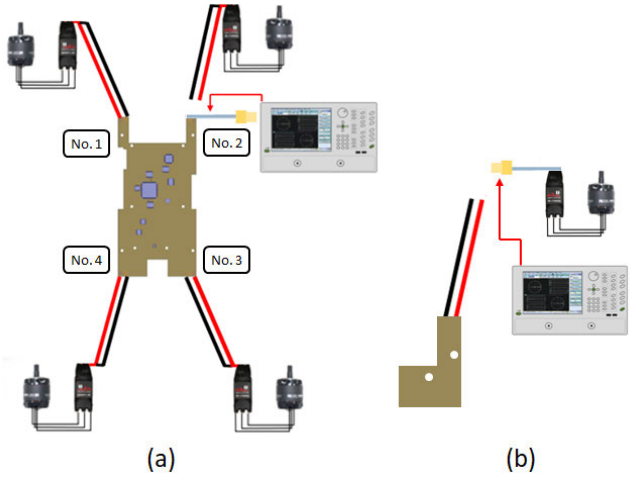

FIGURE 4. (a) Measurement setting for input impedances on the PCB side and (b) measurement setting for input impedances on the motor side.

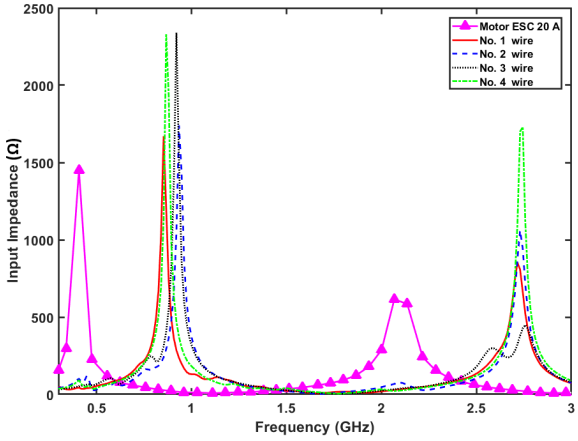

FIGURE 5. Input impedances for PCB side for wires 1 to 4 and motor side.

The input impedance of the motors located at the end of the 2-wire was also measured, as shown in Fig. 4 (b). Because the four motors are identical (model: Air 20 A), the input impedance was measured for only one static motor. This measurement was performed in a similar manner to that discussed above using the VNA.

Distinctly large impedance values were observed for the motors at frequencies of 0.4 GHz and 2.1 GHz, which are different from the corresponding values for the PCB ports, as shown in Fig 5. Based on these measurements, it is possible to infer that the quadcopter drone may be susceptible at specific frequencies, such as 0.4, 0.85, 2.1, and 2.7 GHz.

These resonant frequencies with high impedance values can be changed by modifying the structural and electrical characteristics of the PCB. The structural characteristics of the PCB are illustrated in Fig. 6. The PCB has a four-layer structure, and it consists of an FR-4 substrate ($\epsilon = 4.4$) with horizontal and vertical dimensions of 152 mm and 76 mm, respectively. To validate the changes in resonance frequency caused by the structural characteristics of the PCB,

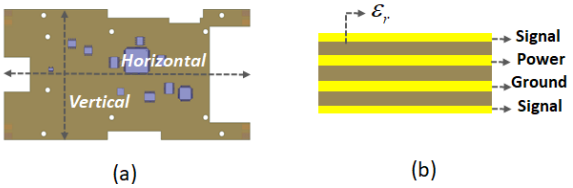

FIGURE 6. PCB information for a quadcopter drone: (a) top view and (b) side view.

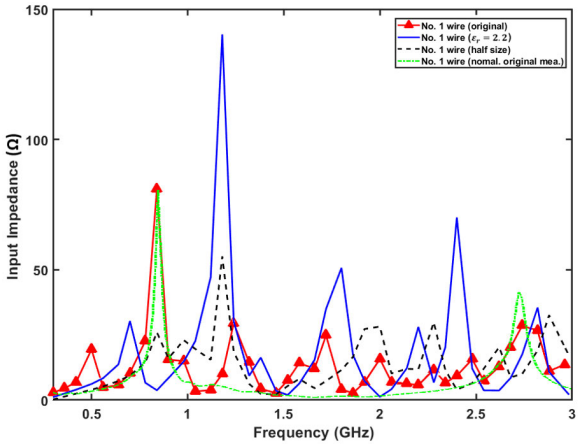

FIGURE 7. Measured and calculated input impedances for no. 1 wire.

3D full-wave EM simulations were performed (HFSS software by ANSYS). In Fig. 7, the solid line with triangle indicates the normalized calculated input impedance of the original PCB structure, revealing strong resonances at approximately 0.85 GHz, which agree well with the measured results. The solid line was obtained by changing the dielectric constant of the PCB substrate from $\epsilon = 4.4$ to $\epsilon = 2.2$. The resulting resonant frequency is shifted to a higher value of 1.2 GHz. It is noteworthy that the resonant frequencies correspond to the second and higher resonant modes of the PCB structure. The dotted line was obtained by changing the horizontal dimension to 76 mm, which is half of the original dimension. The resonant frequency thus increases as a result of the reduced size.

C. SIMULATION OF WIRE COUPLING

To estimate the coupled voltages at both ends of the 2-wire accurately, three-dimensional full-wave EM simulations were performed, as illustrated in Fig. 3. A single-frequency plane wave was used as an incident wave, and Ports 1 and 2 were assigned to the motor and PCB sides, respectively. We assumed that the incident plane wave travels along the horizontal plane of the drone and that the angle between the 2-wire in the drone and the incident wave is 56°, based on the slight asymmetry in the structure. Full-wave simulations were performed in the time domain (XFDTD software by REMCOM). In this study, our simulations focused on specific frequency points, such as 0.4, 0.85, 2.1, and 2.7 GHz, which were shown to produce the maximum coupling effects in Sections II-A and B. The input impedance on the PCB side is 1660 Ω and that on the motor side is 3 Ω at 0.85 GHz. Fig. 8 presents the coupling voltages at both ends of the load on the 2-wire when the EM wave has a magnitude of 50 kV/m belonging to HPEM. On the PCB side, a maximum coupling voltage of 250 V is induced, whereas the motor side exhibits a maximum coupling voltage of less than 10 V. This is because the impedance value on the PCB side is much greater than that on the motor side at a frequency of 0.85 GHz.

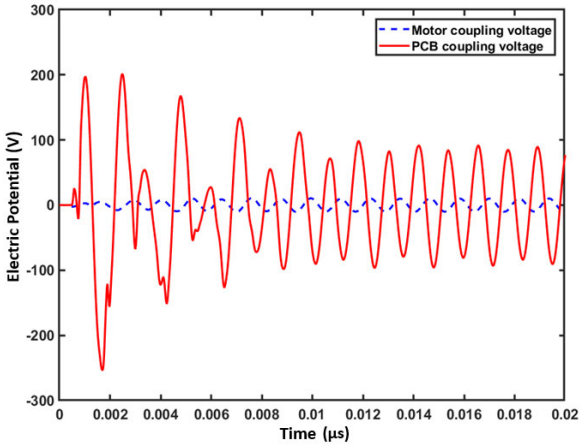

FIGURE 8. Simulation results for coupling voltage {incident frequency = 0.85 GHz} (solid line: PCB side, dotted line: motor side).

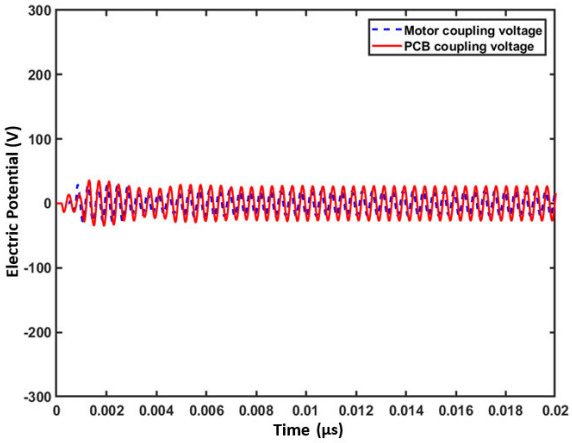

FIGURE 9. Simulation results for coupling voltage {incident frequency = 2.45 GHz} (solid line: PCB side, dotted line: motor side).

When the frequency of the incident wave is 2.45 GHz, the input impedances on the PCB and motor sides are both 15 Ω. Fig. 9 presents the coupling voltages at both ends of the wire with a 50-kV/m incident wave. On the PCB side, a maximum coupling voltage of 43 V was induced, while that on the motor side was only 25 V. According to Equations (1) and (2), the coupling voltages should increase with increasing frequency; however, due to the low impedance value of the PCB side, a low-level coupling phenomenon was observed.

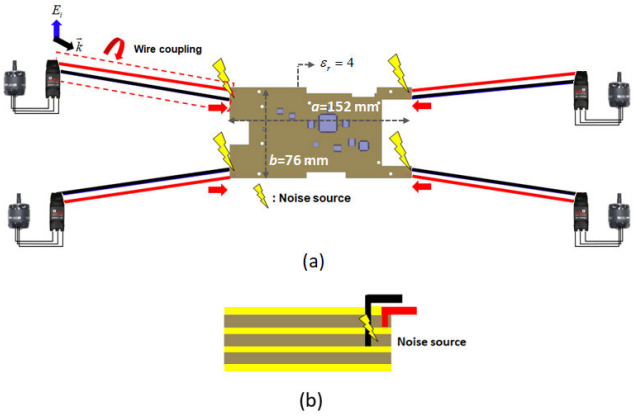

FIGURE 10. (a) Configuration of noise sources in motor power wires and (b) locations of noise sources in the PCB.

III. COUPLING WITH A PCB

A considerably large coupling voltage can be induced by the 2-wires connected to the motors. The quadcopter drone has four motor power wire couples connected to the four edges of the PCB. In other words, as shown in Fig. 10, the induced coupling voltages in the 2-wires can act as noise sources at the four edges of the PCB. Subsequently, these noise sources can affect the IC chips on the PCB and cause malfunctions in the quadcopter drone control system [24]. This section describes full-wave and circuit simulations that were performed to quantify these effects on the IC chips on the PCB.

A. PARALLEL PLATE RESONANCE

Most PCBs have power and ground planes. The quadcopter drone considered in this study, however, utilizes a four-layer PCB containing power and ground planes on the second and third levels. When noise sources are connected to these planes, as illustrated in Fig. 10 (b), they can affect the IC chips on the PCB along with the influence of parallel plate resonance. The parallel plate resonance frequency varies based on the physical dimensions and dielectric material of the PCB, as indicated in Equation (4) for a rectangular structure.

$$f_{r,mn} = \frac{c_0}{2\sqrt{\epsilon_r}}\sqrt{\left(\frac{m}{a}\right)^2 + \left(\frac{n}{b}\right)^2}, \qquad m, n = 0, 1, 2... \quad (4)$$

where a and b are the horizontal and vertical dimensions of the PCB, respectively, and ϵ_r is the relative dielectric constant of the PCB substrate. The PCB used in this study is asymmetric and the resonant frequencies can be calculated using an eigenvalue analysis, as summarized in Table 1. To divide enough meshes for obtaining the exact simulation results, the reference frequency was set to 3 GHz and delta S(represents mesh stability) was set to 0.05. Fig. 11 presents the field distributions of the main PCB for the first few eigenvalues.

Figs. 11 (a), (c), and (d) present the cases of parallel plate resonance at frequencies of 0.5 (eigenmode: 1), 1.78 (eigenmode: 8), and 2.45 (eigenmode: 14) GHz. Fig. 11 (b) presents the case with a frequency of 0.85 GHz, which results in the lowest coupling voltage, as discussed in Section II-C, and exhibits no parallel resonance phenomena. The noise sources with the parallel plate resonance frequencies had a greater influence on the main PCB region compared to those at other frequencies. In the previous section, frequencies of 0.85 GHz and 2.45 GHz were selected for analysis. We will now consider another set of frequencies at 0.5 GHz and 1.78 GHz as cases with a greater influence on the motor control IC chip. In the previous section, it was found that the magnitudes of the coupling voltages in the 2-wire differ depending on the frequency. Therefore, the initial magnitudes of noise sources should be considered to quantify coupling effects. In the following section, the effects of incident EM waves at 0.5, 0.85, 1.78, and 2.45 GHz are compared to derive the relationship between PCB resonance and wire resonance.

TABLE 1. Resonance Modes of a PCB acting as a Parallel Plate.

Eigen mode number	1	2	3	4	5
Resonance frequency (GHz)	0.5	0.8	0.98	1.27	1.29
Eigen mode number	6	7	8	9	10
Resonance frequency (GHz)	1.60	1.78	1.97	2.02	2.18

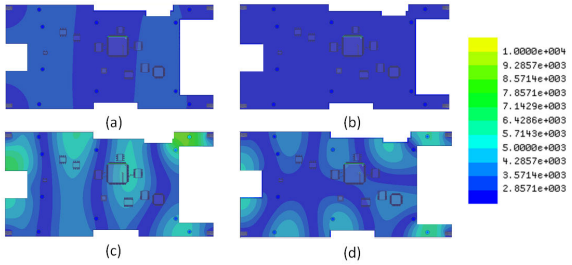

FIGURE 11. Electric field distribution in the PCB: (a) $f = 0.5$ GHz, (b) $f = 0.85$ GHz, (c) $f = 1.78$ GHz, (d) $f = 2.45$ GHz.

B. COUPLING EFFECTS ON IC CHIPS

In this section, the coupling effects of noise sources on the motor control chip (TXS1080) are analyzed. The motor control chip is a critical IC chip for drone operation, as illustrated in Fig. 12. The waveforms of the noise sources were obtained using full-wave simulations, as shown in Fig. 13. The peak magnitude of the noise source is 250 V at 0.85 GHz with values of 6, 67, and 43 V at 0.5, 1.78, and 2.45 GHz, respectively, as derived in the previous section. Simulations were conducted using circuit simulators combined with full-wave analysis to derive the port voltages at the pins of the IC chip in the time domain. Fig. 14 presents the coupling voltage in the motor control chip for different incident waves. For a noise level of 0.85 GHz, a coupling voltage of 130 V was generated at the motor control chip pin. Maximum coupling voltages of 2, 25, and 15 V were induced at 0.5, 1.78, and 2.45 GHz, respectively. Because the greatest coupling voltage

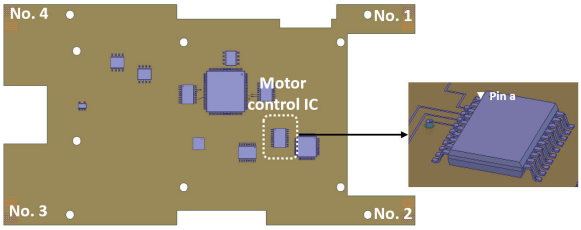

FIGURE 12. Coupling analysis of the motor control IC chip with different noise sources.

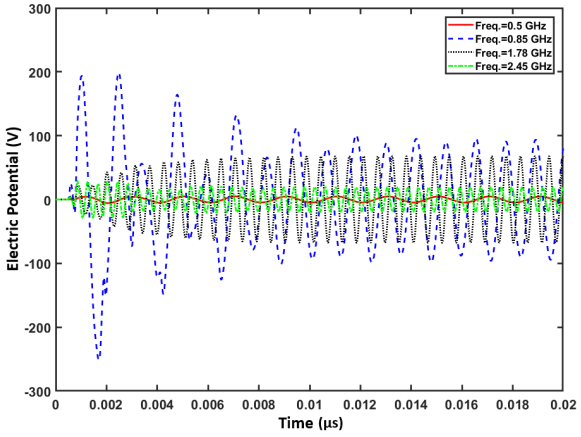

FIGURE 13. Waveforms of noise sources at different frequencies.

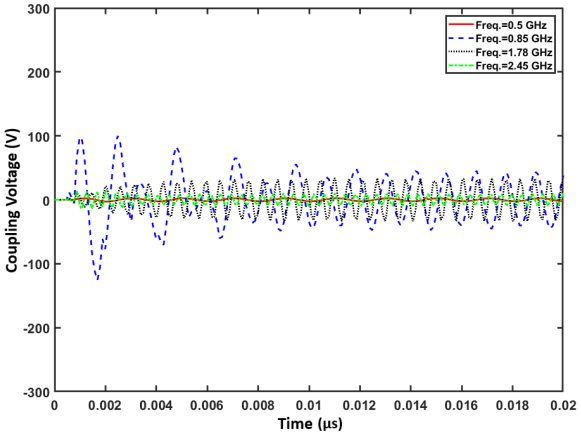

FIGURE 14. Coupling voltage at a pin of the motor control IC chip.

occurs with a 0.85 GHz incident wave, we concluded that system malfunctions could occur at this frequency.

IV. RCS ANALYSIS OF A QUADCOPTER DRONE USING 2D ISAR

In the previous section, coupling effects based on the input impedance of the main PCB and motor were analyzed to predict the vulnerability of a quadcopter drone. In this section, RCS analysis of a quadcopter drone is performed using a 2D ISAR imaging technique. The effects of the motor power wire are analyzed in conjunction with the RCS to determine if greater input impedance values lead to a larger RCS and stronger coupling effects [25].

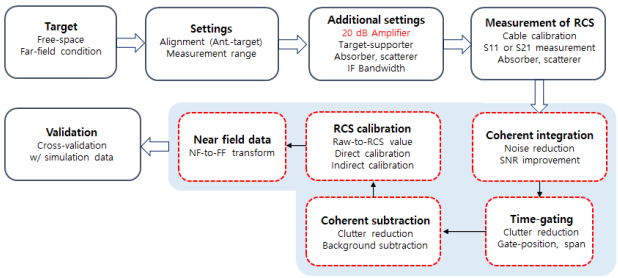

FIGURE 15. Post-processing of RCS measurements of a quadcopter drone.

A. CALIBRATION PROCESS FOR A SMALL RCS OBJECT

Because quadcopter drones have very small RCSs, a careful calibration process must be performed prior to actual RCS measurements, as illustrated in Fig. 15 [26], [27]. Most notably, a 20-dB amplifier is connected to the front of the VNA transmitter (port 2) to increase the transmission power. To verify the accuracy of the measurement procedure, the RCS of a 30 cm PEC sphere was measured and compared with the theoretical value.

Next, to analyze the RCS results of the quadcopter drone, the 2D ISAR technique was applied to the measured RCS data. This technique is based on the inverse Fourier transformation of an electric field extracted from the measured RCS data using Equations (5)–(7) [28].

$$E^s(k,\Phi) = \sum_{i=1}^{N} A_0\, e^{-j2kcos\Phi x_0} e^{-j2ksin\Phi y_0} = \sum_{i=1}^{N} A_0\, e^{-j2kx_0} e^{-j2k\Phi y_0}, \tag{5}$$

$$\mathcal{F}_2^{-1}\{E^s(k,\Phi)\} = \sum_{i=1}^{N} A_0 \mathcal{F}_1^{-1}\{e^{-j2\pi\left(\frac{2f}{c}\right)(x_0)}\} \mathcal{F}_1^{-1}\{e^{-j2\pi\left(\frac{k_c\Phi}{\pi}\right)(y_0)}\}, \tag{6}$$

$$E^s(x,y) = \sum_{i=1}^{N} A_0 \left[\int_{-\infty}^{\infty} e^{-j2\pi\left(\frac{2f}{c}\right)x_0} e^{-j2\pi\left(\frac{2f}{c}\right)x} d\left(\frac{2f}{c}\right)\right] \left[\int_{-\infty}^{\infty} e^{-j2\pi\left(\frac{k_c\Phi}{\pi}\right)y_0} e^{-j2\pi\left(\frac{k_c\Phi}{\pi}\right)y_0} d\left(\frac{k_c\Phi}{\pi}\right)y\right], = A_0\delta(x-x_0, y-y_0), = ISAR(x-x_0, y-y_0), \tag{7}$$

$$\Delta x = \frac{c}{2B}, \tag{8}$$

$$\Delta y = \frac{c}{2f_c\Omega}, \tag{9}$$

where x and y are defined in the physical space, and k and Φ represent the spatial frequency and physical incident angle, respectively. The resolution of the 2D ISAR image is determined from the frequency bandwidth B and total measured angle Ω, as shown in Equations (8) and (9). In particular, k and B represent the distance and resolution of the horizontal axis about the 2D ISAR, and Φ and Ω represent the distance and resolution of the vertical axis about 2D ISAR.

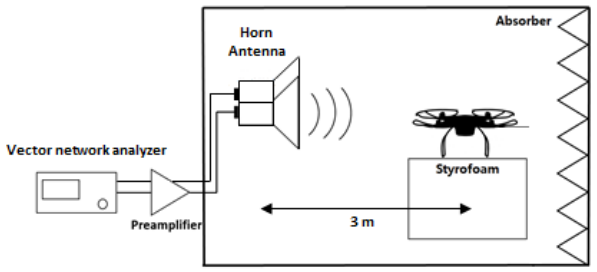

FIGURE 16. Configuration of measurement setup.

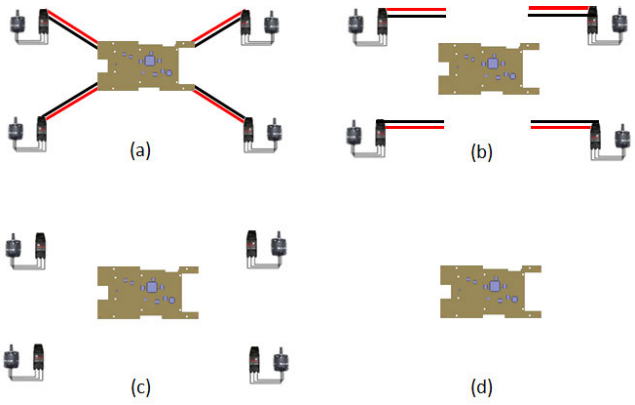

FIGURE 17. (a) Scenario 1 (original quadcopter drone), (b) Scenario 2 (without PCB side), (c) Scenario 3 (without PCB side & motor side), (d) Scenario 4 (removal of all four motors).

B. RCS MEASUREMENT OF THE QUADCOPTER DRONE

Fig. 16 presents the RCS measurement setup for the quadcopter drone. While far-field conditions are satisfied, the measured frequency range and sweep angle range are 0.5–3 GHz and −30°∼30°, respectively. Measurements were performed for four different cases, as shown in Figs. 17 (a)–(d). In the first case, the RCS of the drone with the main PCB and motors connected by motor power wires was measured. For the second case, the motor power wires were disconnected from the main PCB load end. In the third case, the motor power wires were disconnected from the main PCB load end as well as from the motors. In the final case, the motor power wires and motors were removed and the RCS of the remaining structure was measured.

C. ANALYSIS OF THE QUADCOPTER DRONE USING 2D ISAR

Figs. 18–21 present the images of the quadcopter drone obtained using the 2D ISAR technique. These 2D ISAR images were reconstructed from data recorded with a bandwidth of 1 GHz around the center frequencies. Fig. 18 presents the 2D ISAR images for the first measurement scenario. The image of the quadcopter drone becomes increasingly visible as the center frequency increases, but appears to fade above 2.1 GHz, which produces the greatest coupling voltage in the range of 0.5–3 GHz. Both the PCB and motor parts appear to be visible when the center frequency is 2.1 GHz.

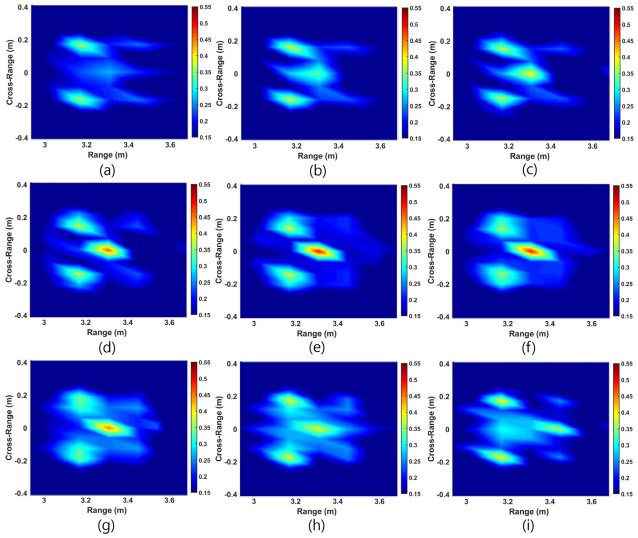

FIGURE 18. 2D ISAR images of quadcopter drone in setting no. 1: (a) center frequency = 1.7 GHz, (b) center frequency = 1.8 GHz, (c) center frequency = 1.9 GHz, (d) center frequency = 2.0 GHz, (e) center frequency = 2.1 GHz, (f) center frequency = 2.2 GHz, (g) center frequency = 2.3 GHz, (h) center frequency = 2.4 GHz, (i) center frequency = 2.5 GHz.

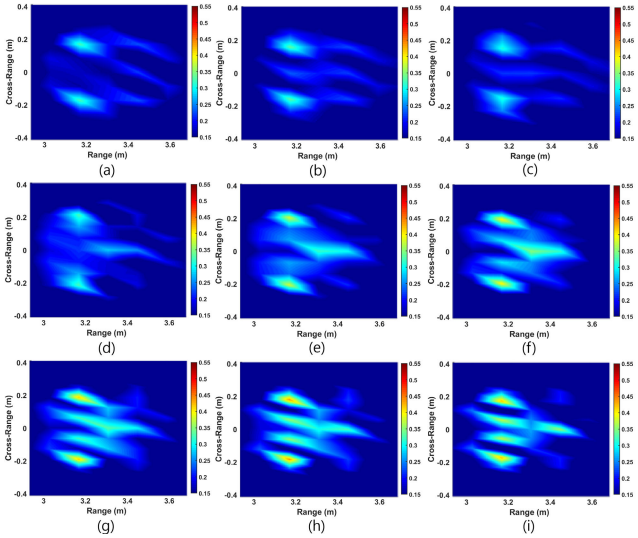

FIGURE 19. 2D ISAR images of quadcopter drone in setting no. 2: (a) center frequency = 1.7 GHz, (b) center frequency = 1.8 GHz, (c) center frequency = 1.9 GHz, (d) center frequency = 2.0 GHz, (e) center frequency = 2.1 GHz, (f) center frequency = 2.2 GHz, (g) center frequency = 2.3 GHz, (h) center frequency = 2.4 GHz, (i) center frequency = 2.5 GHz.

Fig. 19 presents the 2D ISAR images for the second scenario. In this case, the images of the quadcopter drone are less clear than those in the first case, particularly for the PCB. This is because the dominant coupling wires are disconnected from the PCB, resulting in significantly reduced PCB radiation.

Fig. 20 presents the ISAR images for the third scenario. In this case, the images of both the PCB and motor are weaker compared to those in the first scenario. Compared to the second scenario, the effect on the motor is weaker but that on the PCB remains relatively strong. This is caused by the fact that the wires are removed from both the motor side

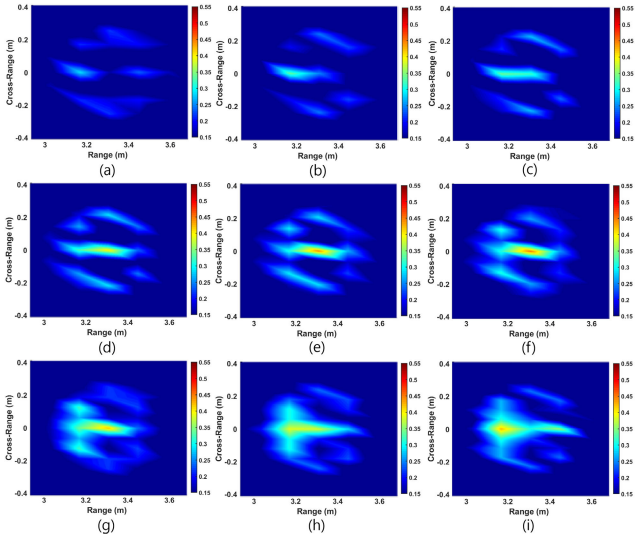

FIGURE 20. 2D ISAR images of quadcopter drone in setting no. 3: (a) center frequency = 1.7 GHz, (b) center frequency = 1.8 GHz, (c) center frequency = 1.9 GHz, (d) center frequency = 2.0 GHz, (e) center frequency = 2.1 GHz, (f) center frequency = 2.2 GHz, (g) center frequency = 2.3 GHz, (h) center frequency = 2.4 GHz, (i) center frequency = 2.5 GHz.

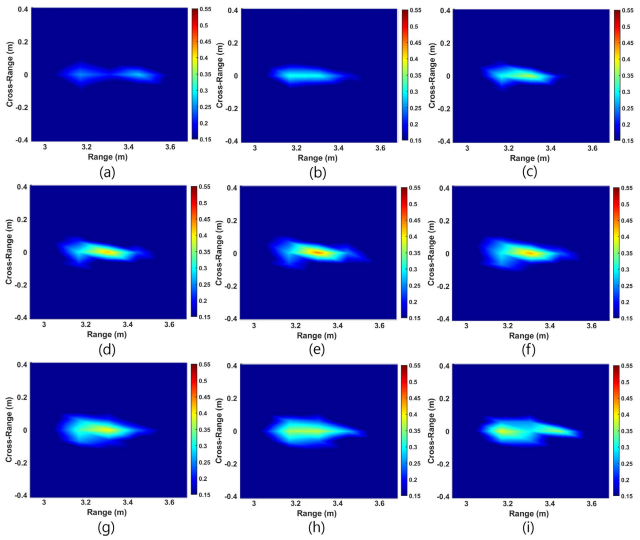

FIGURE 21. 2D ISAR images of quadcopter drone in setting no. 4: (a) center frequency = 1.7 GHz, (b) center frequency = 1.8 GHz, (c) center frequency = 1.9 GHz, (d) center frequency = 2.0 GHz, (e) center frequency = 2.1 GHz, (f) center frequency = 2.2 GHz, (g) center frequency = 2.3 GHz, (h) center frequency = 2.4 GHz, (i) center frequency = 2.5 GHz.

and PCB side. As a result, the RCS of the PCB is larger than those of the isolated motors. Finally, Fig. 21 presents the 2D ISAR images of the fourth scenario. In this case, only the PCB appears in the images.

Clearly, the most significant coupling is generated by the wires, and the wire-coupled voltages and currents are delivered to the loads from the wire ends (i.e., to the motor and PCB). Secondary coupling can enhance the RCS or ISAR signal levels in addition to the primary direct coupling at the motors and PCB.

The scattering effect of the quadcopter drone with and without motor power wires can be shown in Figs. 18–21.

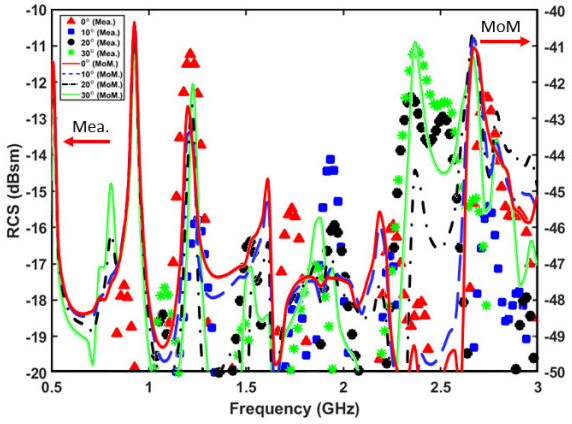

FIGURE 22. Measured and calculated RCS results for scenario 4.

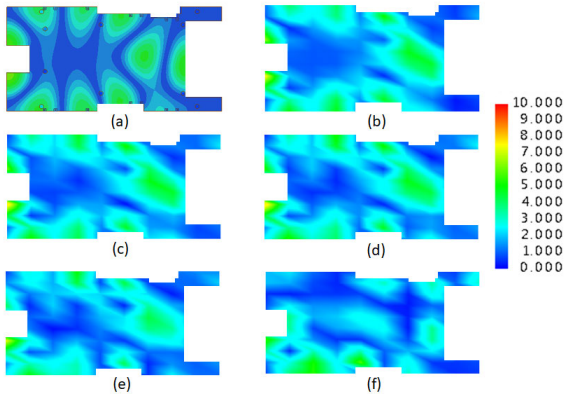

FIGURE 23. Results of near-field: (a) eigen mode no. 15, (b) 0° incident angle, (c) 10° incident angle, (d) 20° incident angle, (e) 30° incident angle, (f) 30° incident angle (2.4 GHz).

In addition, these results present that the high RCS appears around the main PCB when the center frequency is 2.1 GHz. This phenomenon is explained using the RCS results from Scenario 4. Fig. 22 shows the RCS results of the measurement and full-wave simulation (FEKO software by Altair). When the center frequency of ISAR is 2.1 GHz, the RCS value increases at 2.7 GHz for a reduced angle of incidence; the RCS value increases at 2.4 GHz for an increased angle of incidence.

These high RCS values at specific frequencies can be verified by analyzing the near-field results of the simulation of the main PCB, as shown in Fig. 23 for 2.7 GHz. Fig. 23 (a) shows the PCB resonance for eigenmode 15. Fig. 23 (b) shows the near-field result when a plane wave is incident to the main PCB with a 0° angle. The two results show a similar field effect on the main PCB, validating the fact that RCS values are affected by the main PCB resonance at 2.7 GHz. Next, Figs. 23 (c)–(e) show near-field results with the following incidence angles: 10, 20, and 30°, respectively. As the incidence angle changes, the length dimension corresponding to parallel plate resonance slightly changes. As a result, the PCB resonance frequency shifts. Comparing Figs. 23 (e) and (f), we can see that the frequency of maximum RCS shifts from 2.7 to 2.4 GHz.

V. CONCLUSION

In this study, coupling effects of external EM waves on a quadcopter drone were analyzed. We confirmed that the coupling of an EM wave through a quadcopter drone occurs predominantly through the 2-wire power cables connecting the PCB to the motors. The coupling voltages are dependent on the impedance values at both ends of the 2-wires. The induced coupling voltage in this paper can be treated as a noise source, which may affect sensitive IC chips on the PCB. Additionally, we confirmed that the parallel plate resonance of the PCB governs the coupled noise voltage in the internal ports because noise effects can be amplified and exaggerated when resonance frequencies coincide with incident waves.

The RCS of the quadcopter drone was analyzed at various frequencies. Based on four different experimental scenarios, the RCS and resulting ISAR images of the quadcopter drone were measured, and it was confirmed that wire coupling is the dominant cause of secondary effects.

Additionally, wire coupling in a quadcopter drone generates large voltages at specific frequencies due to the generation of high input impedances at both ends of the wires. Furthermore, this study proved that the RCS of a quadcopter drone is large as a result of wire re-radiation. The effects of the load impedances of the motor power wire were systematically modeled based on simulations and measurements, and we subsequently constructed a very effective and accurate analysis framework for complex objects exposed to external EM fields.

REFERENCES

[1] S. Glasstone and P. J. Dolan, "Effects of nuclear weapons," U.S. Dept. Defense, Washington, DC, USA, Tech. Rep. ADA087568, 1977.
[2] M. Seo, S. Chi, Y. Kim, W. Park, H. Kang, and C. Huh, "Electromagnetic wave shielding effectiveness measurement method of EMP protection facility," *J. Korean Inst. Electromagn. Eng. Sci.*, vol. 25, no. 5, pp. 548–558, 2014.
[3] J.-K. Du, J.-W. Ahn, S.-M. Hwang, and J.-G. Yook, "Analysis of coupling effects in waveguides using the BLT equation and numerical methods," in *IEEE MTT-S Int. Microw. Symp. Dig.*, Jun. 2012, pp. 1–3.
[4] J.-K. Du, S.-M. Hwang, J.-W. Ahn, and J.-G. Yook, "Analysis of coupling effects to PCBs inside waveguide using the modified BLT equation and full-wave analysis," *IEEE Trans. Microw. Theory Techn.*, vol. 61, no. 10, pp. 3514–3523, Oct. 2013.
[5] R. B. Schulz, V. C. Plantz, and D. R. Brush, "Shielding theory and practice," *IEEE Trans. Electromagn. Compat.*, vol. EMC-30, no. 3, pp. 187–201, Aug. 1988.
[6] H.-D. Kang, I.-Y. Oh, and J.-G. Yook, "Analytic modeling of oblique penetration of early-time high altitude electromagnetic pulse into dispersive underground multilayer structures," *J. Electromagn. Waves Appl.*, vol. 27, no. 13, pp. 1649–1659, 2013.
[7] Q. F. Liu, W. Y. Yin, M. F. Xue, J. F. Mao, and Q. H. Liu, "Shielding characterization of metallic enclosures with multiple slots and a thin-wire antenna loaded: Multiple oblique EMP incidences with arbitrary polarizations," *IEEE Trans. Electromagn. Compat.*, vol. 51, no. 2, pp. 284–292, May 2009.
[8] S.-Y. Hyun, J.-K. Du, H.-J. Lee, K.-W. Lee, J.-H. Lee, C. Jung, E.-J. Kim, W. Kim, and J.-G. Yook, "Analysis of shielding effectiveness of reinforced concrete against high-altitude electromagnetic pulse," *IEEE Trans. Electromagn. Compat.*, vol. 56, no. 6, pp. 1488–1496, Dec. 2014.
[9] S. Kim, Y. Kim, S.-K. Pang, and J.-G. Yook, "Electromagnetic shielding effectiveness with multi-layered waveguide-below-cutoff array for improved air flow," in *Proc. IEEE Asia–Pacific Microw. Conf. (APMC)*, Nov. 2017, pp. 276–279.
[10] S. Kim, Y. Kim, S.-K. Pang, and J.-G. Yook, "Modified shielding effectiveness equation for novel multilayered waveguide-below-cutoff array," *IEEE Trans. Microw. Theory Techn.*, vol. 66, no. 9, pp. 3912–3920, Sep. 2018.
[11] H. Yang, J. S. Yuan, Y. Liu, and E. Xiao, "Effect of gate-oxide breakdown on RF performance," *IEEE Trans. Device Mater. Rel.*, vol. 3, no. 3, pp. 93–97, Sep. 2003.
[12] K.-A. Lee, J.-H. Rhee, Y.-M. Cho, J.-E. Baek, and K.-C. Ko, "Damage prediction of RF system affected by electromagnetic pulse," in *Proc. Pulsed Power Conf. (PPC)*, Jun. 2013, pp. 1–6.
[13] S.-M. Hwang, J.-I. Hong, S.-M. Han, C.-S. Huh, and J.-S. Choi, "Susceptibility and coupled waveform of microcontroller device by impact of UWB-HPEM," *J. Electromagn. Waves Appl.*, vol. 24, nos. 8–9, pp. 1059–1067, 2010.
[14] M. Ritchie, F. Fioranelli, H. Griffiths, and B. Torvik, "Micro-drone RCS analysis," in *Proc. IEEE Radar Conf.*, Oct. 2015, pp. 452–456.
[15] R. L. Sturdivant and E. K. P. Chong, "Systems engineering baseline concept of a multispectral drone detection solution for airports," *IEEE Access*, vol. 5, pp. 7123–7138, 2017.
[16] T. Li, B. Wen, Y. Tian, Z. Li, and S. Wang, "Numerical simulation and experimental analysis of small drone rotor blade polarimetry based on RCS and micro-Doppler signature," *IEEE Antennas Wireless Propag. Lett.*, vol. 18, no. 1, pp. 187–191, Jan. 2019.
[17] G. Fang, J. Yi, X. Wan, Y. Liu, and H. Ke, "Experimental research of multistatic passive radar with a single antenna for drone detection," *IEEE Access*, vol. 6, pp. 33542–33551, 2018.
[18] A. V. Khristenko, M. O. Konovalenko, M. E. Rovkin, V. A. Khlusov, A. V. Marchenko, A. A. Sutulin, and N. D. Malyutin, "Magnitude and spectrum of electromagnetic wave scattered by small quadcopter in *X*-band," *IEEE Trans. Antennas Propag.*, vol. 66, no. 4, pp. 1977–1984, Apr. 2018.
[19] C. R. Paul, *Introduction to Electromagnetic Compatibility*, vol. 184. Hoboken, NJ, USA: Wiley, 2006.
[20] R. Kanyou Nana, S. Korte, S. Dickmann, H. Garbe, and F. Sabath, "Estimation of the threat of iemi to complex electronic systems," in *Proc. Int. Conf. Electromagn. Adv. Appl.*, Turin, Italy, vol. 7, 2009, pp. 249–253.
[21] M. Leone, "Radiated susceptibility on the printed-circuit-board level: Simulation and measurement," *IEEE Trans. Electromagn. Compat.*, vol. 47, no. 3, pp. 471–478, Nov. 2005.
[22] S. Kim, J. Lee, J.-S. Choi, and J.-G. Yook, "Analysis of electromagnetic pulse coupling into electronic device considering wire and PCB resonance," in *Proc. Int. Symp. Antennas Propag. (ISAP)*, Sep. 2018, pp. 521–522.
[23] O. Fujiwara, K. Nakamura, and J. Wang, "Correspondence between frequency characteristics of radiated emission and input impedance of power-ground planes of pcb," *IEICE Trans. Commun.*, vol. J86-B, no. 8, pp. 1639–1646, Aug. 2003.
[24] T.-L. Wu, S.-T. Chen, J.-N. Huang, and Y.-H. Lin, "Numerical and experimental investigation of radiation caused by the switching noise on the partitioned DC reference planes of high speed digital PCB," *IEEE Trans. Electromagn. Compat.*, vol. 46, no. 1, pp. 33–45, Feb. 2004.
[25] C. W. Trueman, S. R. Mishra, S. J. Kubina, and C. L. Larose, "RCS of resonant scatterers with attached wires," *IEEE Trans. Antennas Propag.*, vol. 41, no. 3, pp. 351–354, Mar. 1993.
[26] S. K. Wong, E. Riseborough, G. Duff, and K. K. Chan, "Radar cross-section measurements of a full-scale aircraft duct/engine structure," *IEEE Trans. Antennas Propag.*, vol. 54, no. 8, pp. 2436–2441, Aug. 2006.
[27] M. Potgieter, J. W. Odendaal, C. Blaauw, and J. Joubert, "Bistatic RCS measurements of large targets in a compact range," *IEEE Trans. Antennas Propag.*, vol. 67, no. 4, pp. 2847–2852, Apr. 2019.
[28] C. Ozdemir, *Inverse Synthetic Aperture Radar Imaging With MATLAB Algorithms*. Hoboken, NJ, USA: Wiley, 2012.

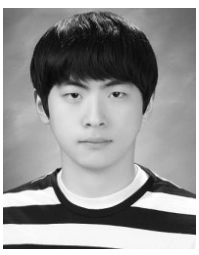

SANGIN KIM (S'15) received the B.S. degree from Yonsei University, Seoul, South Korea, in 2015, where he is currently pursuing the Ph.D. degree, all in electrical and electronics engineering.

His current research interests include HEMP, electromagnetic shielding analysis, plasma analysis, vital sign sensor, and radio-frequency systems. His recent research focuses on electrical problems caused by HEMP.

YEONG-HOON NOH received the B.S. degree from Yonsei University, Seoul, South Korea, in 2017, where he is currently pursuing the Ph.D. degree, all in electrical and electronics engineering.

His current research interests include RCS, numerical electromagnetics, and design and analysis of microwave structure. His recent research focuses on RCS measurement for structure of various shapes.

JINHYO LEE received the B.S. degree in industrial engineering from Korea Air Force Academy, Cheongju, South Korea, in 2009. He is currently pursuing the M.S. degree in electrical and electronics engineering with Yonsei University.

His current research interests include HEMP, anti-drone, and wire coupling effects. His recent research focuses on electrical problems caused by HEMP.

JONGWON LEE (S'09–M'11) received the B.S. degree in electrical engineering from Seoul National University, Seoul, South Korea, in 2002, and the M.S. and Ph.D. degrees from Purdue University, West Lafayette, IN, USA, in 2007 and 2010, respectively, all in electrical and computer engineering.

He was a System Programmer with Chosun-Ilbo, Seoul, from 2002 to 2005. In 2011, he joined the Agency for Defense Development, Daejeon, South Korea, where he is currently a Senior Researcher. His current research interests include computational electromagnetics of circuit design and analysis of high-power microwave systems.

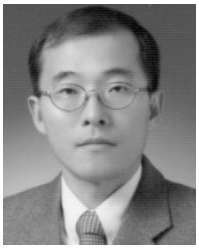

JIN-SOO CHOI was born in Seoul, South Korea, in 1964. He received the B.S., M.S., and Ph.D. degrees from Yonsei University, Seoul, in 1986, 1989, and 2001, respectively, all in physics.

He has been with the Agency for Defense Development (ADD), Daejeon, South Korea, since 1991, where he is currently a Principal Researcher. In 2003 and 2004, he was with the Naval Research Laboratory, Washington, DC, USA, as a Visiting Scientist. His current research interests include explosion phenomena, high-power electromagnetic sources, and electromagnetic effects.

JONG-GWAN YOOK (S'89–M'97–SM'12) was born in Seoul, South Korea. He received the B.S. and M.S. degrees from Yonsei University, Seoul, in 1987 and 1989, respectively, all in electronics engineering, and the Ph.D. degree from the University of Michigan, Ann Arbor, MI, USA, in 1996.

He is currently a Professor with the School of Electrical and Electronic Engineering, Yonsei University. His research team recently developed various biosensors, such as carbon-nanotube RF biosensors for nanometer-size antigen-antibody detection and remote wireless vital signal monitoring sensors. His current research interests include theoretical/numerical electromagnetic modeling and characterization of microwave/millimeter-wave circuits and components, design of radio-frequency integrated circuits (RFICs) and monolithic microwave integrated-circuits (MMICs), and analysis and optimization of high-frequency high-speed interconnects, including signal/power integrity (EMI/EMC), based on frequency-and-domain full-wave methods.